Detailed characterization of slow and dispersive propagation near a mini-stop-band of an InP photonic crystal waveguide.

Marcelo Davanço[1], Aimin Xing[1], James Raring[2], Evelyn L. Hu[1,2], Daniel J. Blumenthal[1]

[1] *Dept. of Electrical and Computer Engineering, University of California Santa Barbara, Santa Barbara CA 93106.*
[2] *Materials Dept.,, University of California Santa Barbara, Santa Barbara CA 93106.*
mdavanco@ece.ucsb.edu

Abstract: An experimental study of light propagation near a small band gap for a lattice-of-holes InP photonic crystal waveguide is reported. Polarization-resolved measurements of power transmission, reflection and group delay clearly reveal the PC waveguide filtering properties. Group delay enhancement was observed close to the band-edges together with very large dispersion. The test devices were fabricated with a novel technique that allows incorporation of deeply-etched photonic crystals within an InP photonic integrated circuit.

OCIS codes: (130.0130) Integrated Optics; (230.7380) Channel Waveguides

References and links

1. T. J. Karle, Y. J. Chai, C. N. Morgan, I. H. White, and T. F. Krauss, "Observation of Pulse Compression in Photonic Crystal Coupled Cavity Waveguides," J. Lightwave Technol. **22** 514-519 (2004).
2. A. Xing, M. Davanço, S. Camatel, D. J. Blumenthal, E. L. Hu, " Pulse compression in Line Defect Photonic Waveguide ," in Proceedings of the Optical Fiber Communications Conference 2005, Paper OWD5.
3. M. Notomi, K. Yamada, A. Shynia, J. Takahashi, C. Takahashi, I. Yokohama, "Extremely Large Group-Velocity of Line-Defect Waveguides in Photonic Crystal Slabs," Phys. Rev. Lett **87** 253902-1-4 (2001).
4. S. Olivier, H. Benisty, C. Weisbuch, C. J. M. Smith, T. F. Krauss, R. Houdré , "Coupled-mode theory and propagation losses in photonic crystal waveguides," Opt. Express **11** 1490 (2003), http://www.opticsexpress.org/abstract.cfm?URI=OPEX-11-13-1490.
5. S. Olivier, H. Benisty, C. J. M. Smith, M. Rattier, C. Weisbuch, T. F. Krauss, 'Transmission properties of two-dimensional photonic crystal channel waveguides," Opt. Quantum Electron. **34** 171-181 (2002).
6. J. M. Bendickson, J. P. Dowling, M. Scalora, "Analytic expressions for the electromagnetic mode density in finite, one-dimensional, photonic band-gap structures," Phys. Rev. E **53**, 4107 (1996).
7. H. Benisty, Ph. Lalanne, S. Olivier, M. Rattier, C. Weisbuch, C. J. M. Smith, T. F. Krauss, C. Jouanin, D. Cassagne, 'Finite-depth and intrinsic losses in vertically etched two-dimensional photonic crystals," Opt. Quantum Elec. **34** 205-215 (2002).
8. M. L. Mašanović, V. Lal, J. A. Summers , J. S. Barton, E. J. Skogen, Rau, L. G., L. A. Coldren and D. J. Blumenthal, "Widely-Tunable Monolithically-Integrated All-Optical Wavelength Converters in InP," J. Lightwave Technol. **23** 1350-62 (2005).
9. S. Mankopf, R März, M Kamp, D. Guang-Hua, F. Lelarge, A. Forchel, "Tunable photonic crystal coupled-cavity laser," IEEE Jour. Quantum Elec. 40, 1306-14 (2004).
10. A. Xing, M. Davanço, D. J. Blumenthal, E. L. Hu, "Fabrication of InP-based two-dimensional photonic crystal membrane," J. Vac. Sci. Technol. B **22** 70 (2004).
11. T. Jensen, E. Witzel, A. Paduch, P. Ziegler, E.U.Wagemann and O. Funke, "A new method to determine loss, PDL, GD and DGD of passive optical components", 18th NFOEC, Dallas, September 2002.
12. E. Collett, *Polarized Light in Fiber Optics* (The PolaWave Group, 2003), Chap. 13.
13. K. Yamaguchi, M. Kelly, G. Stolze, D. Kobasevic, "Polarization-Resolved Measurements using Mueller Matrix Analysis," Agilent application note 5989-1261EN.
14. The MIT Photonic-Bands package, http://www.ab-inito.mit.edu/mpb/
15. M. Qiu, "Effective index method for heterostructure-slab-waveguide-based two-dimensional photonic crystals," App. Phys. Lett. **81** 1163 (2002).
16. L. J. Gamble, W. M. Diffey, S. T. Cole, R. L. Fork, D. K. Jones, T. R. Nelson, Jr., J. P. Loehr, J. E. Ehret, "Simultaneous measurement of group delay and transmission of a one-dimensional photonic crystal," Opt. Express **5** 267 (1999), http://www.opticsexpress.org/abstract.cfm?URI=OPEX-5-11-267.

#7340 - $15.00 USD Received 2 May 2005; revised 10 June 2005; accepted 13 June 2005

17. G. von Freymann, S. John, S. Wong, V. Kitaev, G. A. Ozin, "Measurement of group velocity dispersion for finite size three-dimensional photonic crystals in the near-infrared spectral region," App. Phys. Lett. **86** 053108 (2005).
18. L. A Coldren and S. W. Corzine, *Diode Lasers and Photonic Integrated Circuits* (Wiley Intersciences), Chap. 6.
19. P. St. Russel, "Bloch wave analysis of dispersion and pulse propagation in pure distributed feedback structures," Jour. Modern Optics **38** 1599-1619 (1991).
20. N. M. Litchinitser, B. J. Eggleton, D. B. Patterson, " Fiber Bragg Gratings for Dispersion Compensation in Transmission: Theoretical Model and Design Criteria for Nearly Ideal Pulse Recompression," J. Lightwave Technol. **15** 1303 (1997).

1. Intoduction

Photonic Crystal (PC) waveguides of the lattice-of-holes type have been shown to offer very interesting light propagation characteristics, given the availability of very slow and dispersive modes in the vicinity of band-gaps [1, 2, 3]. Calculated Bloch-mode group velocities do tend to zero very quickly as band gap frequencies are approached. However, inasmuch as finite PC waveguides can be modeled as 1D-periodic systems in the vicinity of certain band-gaps [4, 5], their transmission characteristics are expected to present only finite group delay peaks near such gaps, accompanying resonances in transmitted and reflected power [6]. In what follows, we present experimental data clearly showing these propagation characteristics near a mini-stop-band of a $W3^{(M)}$ line-defect waveguide [5], such as shown in Fig. 1(a). In order for the characterization to be performed, a novel fabrication platform for photonic integrated circuits incorporating photonic crystals was developed.

2. Description of the tested devices

A series of 20μm×80μm mesas were fabricated, on top of which PC patterns were to be etched. The mesas were accessed via input and output 3-μm wide, 710-μm long weakly-guiding ridge waveguides, as shown in Fig. 1(b). Tilted waveguide designs were used to suppress reflections into the fundamental waveguide mode at the semiconductor/air interface.

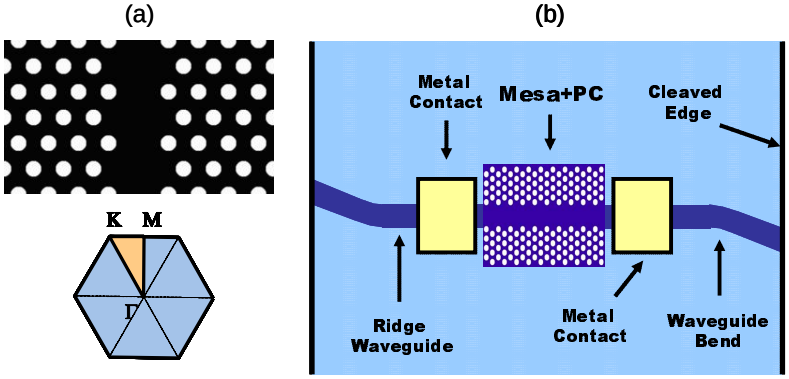

Fig. 1. (a) $W3^{(M)}$ waveguide. The first triangular lattice Brillouin zone is displayed underneath. (b) Top-view schematic of fabricated devices.

All measured PC patterns were 80-μm-long $W3^{(M)}$ line-defect waveguides of varying lattice constant *a* and air-filling fraction; such waveguides are defined by suppressing three lines of holes along the ΓM direction from a triangular-lattice-of-holes PC. The channel widths were on the order of 400nm. As will be shown later, these waveguides display a small band-gap for guided TM modes near the Brillouin-zone boundary. The mechanism responsible for slow and dispersive propagation near this band-gap is the coupling between forward- and backward-propagating waves caused by the periodicity along the waveguide; the same effect takes place at the band-edges near the Brillouin-zone boundary in the PC line-defect waveguides studied in [2, 3, 4, 5]. On the other hand, the advantages of studying this

#7340 - $15.00 USD Received 2 May 2005; revised 10 June 2005; accepted 13 June 2005

effect in the present W3$^{(M)}$ waveguides are the following: firstly, the guided TM modes exist in a range of frequencies where only unconfined, very lossy TE modes exist; thus collected light at the output of the device is mostly TM-polarized and the task of discerning TE and TM curves is thereby much facilitated. Secondly, guided-mode propagation losses are expected to be reasonably low in a three-line-defect waveguide, given the lesser interaction with the holes. Indeed, the observed insertion loss (~ 30dB in the transmission pass-bands) was low enough for the test instruments to yield reliable and repeatable measurements.

The devices were processed on an MOCVD-grown wafer encompassing an n-doped InP substrate, a 1.37Q, 300-nm-thick intrinsic InGaAsP guiding layer, a 1-μm, p-doped InP cladding layer, a 100-nm layer of highly p-doped InGaAs for the formation of ohmic contacts and finally a 50-nm InP cap layer. The approximate refractive index of the guiding layer is 3.45 at λ=1.5μm. Figure 2(a) shows a schematic of an access ridge waveguide, detailing the epitaxial layer-structure. Notice that a p-i-n junction is formed between the top of the ridge and the n-doped substrate.

The upper cladding layer thickness reflects a compromise between achievable etched hole depth and losses at the highly-conductive p-doped InGaAs layer: our dry-etching technique yielded at most 2-μm deep holes, which demanded a thinner upper cladding; as detailed in [7], PC holes should extend far enough into the substrate in order to keep propagation losses due to out-of-crystal-plane radiation as low as possible. Shallow holes will cause the field to leak considerably into the substrate. On the other hand, it was desired to minimize the interaction of the waveguide mode's evanescent tail with the top InGaAs layer and p-doped InP, thereby requiring a thicker cladding.

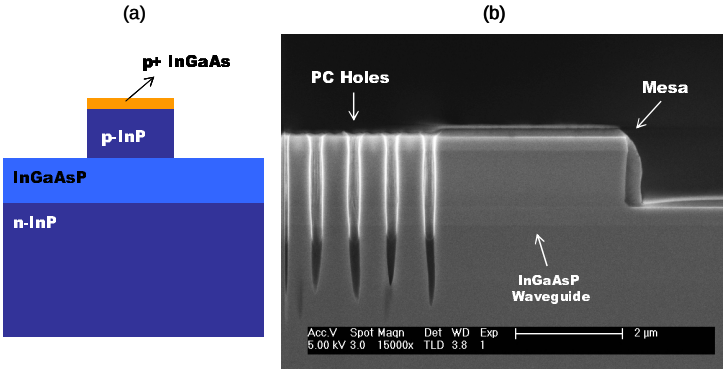

Fig. 2. (a) Schematic cross-section of a ridge waveguide, showing the different waveguide layers. Mesas have the exact same structure. (b) SEM micrograph of a mesa cross section, showing etched photonic crystal holes.

Electrical contacts were defined on the ridge waveguides such that guided light could be detected by measuring current from reverse-biased p-i-n junctions. This facilitated immensely the coupling of ridge waveguides with lens-fibers during the testing process; optimal alignment is in fact achieved in little more than a minute, requiring no equipment other than a voltage-source with a built-in amp meter. An additional reason for the inclusion of the metal contacts was to demonstrate the ability of fabricating devices with electrically-pumped active or passive waveguides, such as described in [8], that incorporate photonic crystals. The present fabrication platform is in fact an extension of the platform used in the latter cited reference.

3. Test-device fabrication

The fabrication process reported here is a novel form of integration of deeply-etched PC with standard photonic integrated circuit structures [8, 9]. Ridge waveguides and mesa patterns were defined initially on a SiN mask layer by contact photolithography. The pattern was transferred to the SiN mask by Reactive Ion Etching (RIE) in a CF_4:O_2 plasma. Next they

#7340 - $15.00 USD Received 2 May 2005; revised 10 June 2005; accepted 13 June 2005

were transferred into the upper cladding layer by RIE using a Methane-Hydrogen-Argon (MHA) mixture, followed by a $HCl:H_3PO_4$ wet-etching step. A 400-nm SiO_2 mask layer was next deposited on the sample. A planarization step with PMGI followed, and mesa tops were exposed by etching down the polymer surface in an oxygen plasma [10]. Electron-beam lithography followed to define PC patterns on top of the mesas. Patterns from the resist were transferred to the SiO_2 mask with a CHF_3 plasma in a Panasonic E640 Inductively-Coupled Plasma (ICP) etcher, then onto the semiconductor with a Unaxis Versalock ICP etcher, using a Cl_2:Ar 1:5 chemistry at 1.5 mT, 200^{o}C. The latter etch was long enough to yield holes extending through the upper cladding and waveguide layers, then about 1μm into the substrate. An SEM picture of one of the PC patterns' cross-section is displayed in Fig. 2(b). A semi-self-aligned resist etch-back technique was used to create openings for contacts on the remaining SiO_2 and SiN layers on selected, lithographically-defined portions of the ridge waveguides. This step is as follows: PMGI is spun and planarized on the surface, followed by spinning of AZ4110 photoresist. Optical lithography is used to define openings on the latter, on top of selected waveguide regions. The AZ400K developer used does not attack the underlying PMGI layer. Dry etching with oxygen plasma is next used to etch-back the exposed PMGI regions until only the waveguide tops are exposed. The SiO_2 and SiN on top of the guides are finally etched in a CHF_3 plasma.

Following these steps, metallic contacts were defined with contact photolithography followed by Ti/Pt/Au e-beam evaporation. The sample was subsequently thinned-down and metallization of the back-side was performed before cleaving.

4. Device measurement and characterization

An Agilent 81910 All-Parameter Analyzer was used to characterize the devices. The measurement system consists of a tunable, low-noise laser source together with a polarization controller and a set of high-speed photodiodes [11]. Müller matrices for a passive device are produced by the instrument through standard techniques [12, 13] and swept-wavelength interferometry [11] is used to yield group delay measurements. Müller matrices fully characterize polarization-dependent transmission through an optical system at fixed wavelengths, relating input and output polarization states. A detailed account of Müller matrices and their properties and applications can be found in [12]. Their use in the present work allowed for a straightforward discernment of TE- and TM-polarized wave transmission from a single measurement run. Application of this technique required attention to aspects discussed in the next paragraph.

The Polarization-Dependent Loss (PDL) of an optical system is defined as $10 \cdot log(I_{max}/I_{min})$, where I_{max} and $I_{\min}$ are the maximum and minimum output intensities with respect to the input State of Polarization (SOP). The Principal States of Polarization (PSP) are the SOP that produce I_{max} and I_{min} and can be obtained from the system's Müller matrix at each wavelength. When measuring a semiconductor device that carries both TE and TM modes, it is reasonable to assume that the two PSP excite either one of these two polarizations at wavelengths where very high PDL is observed [13]. As such, in order to obtain the TE and TM transmission and reflection curves presented below, PSP were obtained at wavelengths with large PDL in each case and applied to the corresponding Müller Matrices at all other wavelengths.

Coupling to the fabricated devices was done by aligning lens-fibers to the input and output waveguides; electrical contacts were biased at -2V with a Keithley 2400LV sourcemeter, and the photocurrents produced by a 0.8-mW optical signal at 1520nm were on the order of 15μA. The optical signal absorption for such bias level was below 0.5dB, measured with an optical power-meter. In each measurement, after the alignment was optimized, the bias voltage was set to zero so light would suffer no extra absorption in the waveguide.

The correct correspondence between measured curves and polarization states was primarily verified by infrared imaging of the output waveguide signals through a free-space polarizer. Additionally, we compared experimental results with effective 2D PC band

#7340 - $15.00 USD Received 2 May 2005; revised 10 June 2005; accepted 13 June 2005

structures, calculated with the 2D Plane-Wave Expansion (PWE) method [14]. The effectiveness of this technique has been experimentally demonstrated in various articles, including [4, 5, 7]; additionally, it has been detailed in [15] that band-structures of 3D lattice-of holes PC with weak vertical confinement and deep holes can be very well approximated by band structures of effective 2D PC. Figure 3(a) shows band diagrams for TM modes of a waveguide with r/a = 0.265 (r being the hole radius) and background index n_{TM} = 3.26 (equal to the effective index of the epi-wafer's first TM slab mode at λ=l.55μm). The color scale corresponds to the electric field energy within the line-defect region, normalized to the total power in the unit cell. Well-confined modes (darker dots) with even symmetry yield higher transmitted output power; two bands of such modes are clearly distinguishable, presenting a small band gap at the Brillouin-zone boundary, around a/λ≈0.275. This band-gap clearly corresponds to the stop-band found in the transmission curves shown in Fig. 3(b). Modes on the high-frequency band are well confined, while those on the low-frequency side are more spread out in the crystal region. It is expected that the latter will suffer higher losses, as a result of a larger interaction with holes. Notice that confined modes are of the index-guided type [6], since a bulk-crystal band gap does not exist for TM modes in the present case.

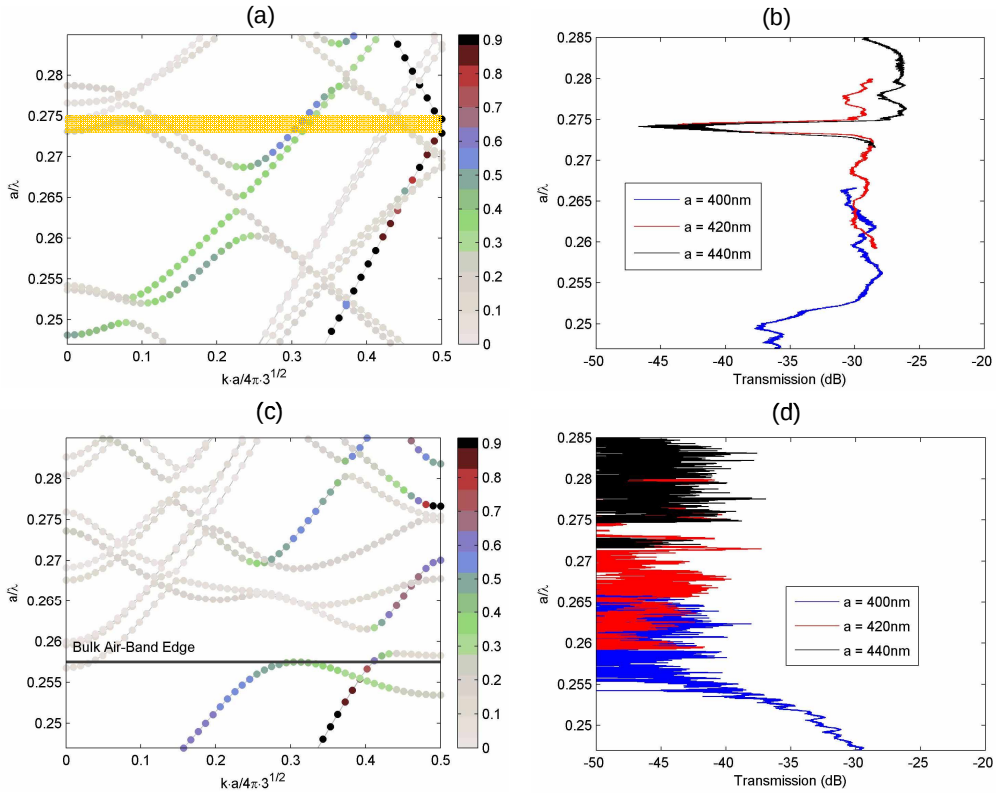

Fig. 3. (a) Band structure for TM modes of a W3$^{(M)}$ waveguide with r/a=0.265 and n=3.26. The yellow shaded area indicates the mini-band-gap position. (b) Corresponding TM transmission curves for devices with a=400nm, a=420nm, and a=440nm. (c) Band structure for TE modes. The bulk-crystal air-band edge is depicted as a continuous line. (d) Corresponding TE transmission curves for the same devices. In both (a) and (c), the color scale relates to the electric field energy confined in the defect region.

Figure 3(c) shows the TE-mode band structure for the same waveguide with background refractive index n_{TE} = 3.28 and Fig. 3(d) shows the corresponding transmission curve. A high-confinement band below a/λ≈0.255 in Fig. 3(c) corresponds to the transmission band on Fig. 3(d). The inexistence of highly-confined modes in the region above a/λ≈0.255 explains the

#7340 - $15.00 USD Received 2 May 2005; revised 10 June 2005; accepted 13 June 2005

low transmitted power in this range in Fig. 3(d). A very small band of highly-confined modes exists near $a/\lambda \approx 0.275$. Transmitted power carried by these is expected to be very low, given their closeness to the Brillouin zone boundary and the narrow width of the band.

It must be pointed out that the substrate light-line in all cases meets the Brillouin-zone boundary at $a/\lambda \approx 0.09$ thus all displayed modes are expected to leak into the substrate.

4.1 TM transmitted and reflected power

The TM transmission PDL is more than 20dB at all wavelengths except within the stop-bands for all measured devices; PSP at λ=1520nm and 1580nm were used to generate transmission curves respectively for a=420nm and a=440nm. For reflection, PSP at λ=1532nm and λ=1610nm were chosen, with PDL≈10dB. The raw reflected signal curve presented a series of 0.4-nm-period oscillations caused by a beating of reflected light from the wafer facet and the PC waveguide input. To suppress this effect, the raw signal was filtered with a 51-sample (500pm) Locally Weighted Scatter Plot Smooth (LOWESS) filter.

Black lines in Fig. 4 show the obtained TM transmittance and reflectance close to the mini-stop-band of representative devices with a=420nm and a=440nm, normalized to their respective maxima. An approximately 10-nm stop-band is observed centered at λ≈1533nm for the first device and at λ≈1607nm for the latter, both corresponding to $a/\lambda \approx 0.274$. The less pronounced resonances on the right side of the stop-bands can be explained by the predicted higher losses. The wide stop-band in transmission corresponds to a high-reflection band. Also, maxima in the transmission curves coincide with minima in reflection. These resonances are due to the finite extent of the PC waveguide [6].

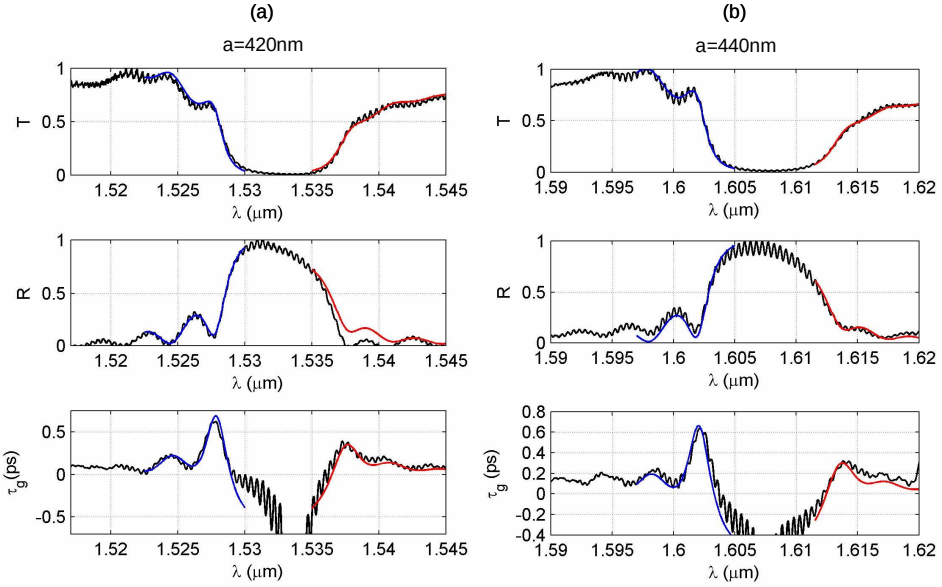

Fig. 4. Transmission (T), reflection (R) and excess group delay (τ_g) for waveguides with two different lattice constants. Black curves are experimental, blue and red are fitted. (a) a=400nm. (b) a=420nm.

4.2 Group delay

Group delay curves for the transmitted signal were obtained from the same instrument [11] for a fixed polarization state at the input. Before the measurement was taken, the power in the pass-bands (determined from the previous transmission measurements) was maximized by tuning a polarization controller inserted before the input fiber. This procedure assured that mostly TM modes were being excited in the input waveguide. At each wavelength, a 100-sample averaging was used for accuracy. The same measurement was performed for a regular

#7340 - $15.00 USD Received 2 May 2005; revised 10 June 2005; accepted 13 June 2005

ridge waveguide on the same wafer. The displayed group delay curves are obtained by subtracting the ridge waveguide results from those of the PC waveguides; the displayed values are thus of *excess* group delay. Cavities between the air-facet and ridge-PC waveguide interfaces caused a series of resonant peaks in the measured curves. Smoothing with a 101-sample (1nm) LOWESS filter revealed the PC waveguide group delay structure alone. Figures 4(a) and 4(b) show measured group delay for the same devices as in the previous section. The oscillatory profile with maxima at the first reflectivity minimum is due to the finite extent of the waveguides, as detailed in [6]. Similar group delay curves were experimentally observed in a multilayer GaAs PC [16] and more recently in a silica colloidal PC [17]. The peak excess group delay is $\tau_g \approx 0.62$ps for a=420nm and 0.65ps for a=440nm. The group delay enhancement over that experienced through a ridge waveguide of the same length is of about 60%.

4.3 Fitting with coupled-mode theory

As in [4], propagation close to the mini-stop-band can be reasonably well-described with 1D Coupled-Mode Theory (CMT). Details of the theory can be found in a large number of textbooks, a good example of which is reference [18]. In its basic form, it describes the evolution of an optical wave as it travels along a medium with periodic refractive index perturbation. The periodicity of the perturbation causes coupling between a forward-propagating wave and a backward-propagating counterpart, at frequencies close to where the Bragg condition is satisfied. A transmission stop-band is observed centered at the Bragg frequency, due to a strong energy transfer from the impinging wave into its backward-traveling counterpart. The propagation characteristics of both waves are clearly dependent on the coupling strength between the two and detuning from the Bragg frequency. The theory predicts the following equations for transmission and reflection coefficients of a finite 1D periodic medium:

$$t = \frac{2\sigma}{(z+\sigma)e^{+\sigma L} - (z-\sigma)e^{-\sigma L}} \tag{1}$$

$$r = \frac{2i\,|\kappa|\sinh(\sigma L)}{(z+\sigma)e^{+\sigma L} - (z-\sigma)e^{-\sigma L}} \tag{2}$$

In these equations, κ is the coupling coefficient, $z = \alpha + i\cdot(\beta-\beta_0)$, $\sigma^2 = \kappa^2+z^2$, α and β the loss and propagation constants for both forward- and backward-propagating modes and L is the total length. Also $\beta=2\pi n/\lambda$, and n is the effective phase index, which describes the spatial phase evolution of the field in an unperturbed medium. Notice that material absorption and out-of plane radiation, either intrinsic or caused by hole imperfections can be phenomenologically modeled by the loss parameter.

In the spirit of [4], CMT curves were fitted to the experimental data to yield estimates of coupling strength and propagation losses in the waveguides. In the present case, coupling happens between modes of the same order. Bloch modes on the two sides of the stop-band are considerably different, though, and thus require different fitting parameters.

A least squares fitting algorithm was used to fit the experimental transmission curves of all devices using n, α and κ as parameters. The phase index n was allowed to change within 10% of the values calculated from the PWE calculation [4]. Fitted curves for the devices shown in Fig. 4 are displayed in red and blue. Fitting values obtained from four devices with a=420nm and slightly different filling fractions were in the ranges n=3.5±0.1, α=(41.8±4.15)cm^{-1}, κ=(4.3±0.3)×10^{2}cm^{-1} on the high-frequency band-edge; on the low-frequency edge, n=3.7±0.2, α=(77.2±2.4)cm^{-1}, κ=(3.7±0.1)×10^{2}cm^{-1} were obtained. Five devices with a=440nm and slightly different filling fractions yielded parameters in the ranges n=3.5±0.1, α=29.8±4.9cm^{-1}, κ=(3.9±0.3)×10^{2}cm^{-1} on the high-frequency side and n=3.7±0.1, α=90±1.2cm^{-1}, κ=(4.1±0.4)×10^{2}cm^{-1} on the low-frequency side. The spread in phase index and coupling coefficients can be attributed to the differing filling fractions and hole quality, as well as noise in the experimental data. Additionally, the CMT model used assumes uniform

#7340 - $15.00 USD Received 2 May 2005; revised 10 June 2005; accepted 13 June 2005

reflectivity and coupling coefficient distribution along the crystal, while the devices' filling-fractions vary slightly along the PC waveguide. The PC lithography was realized without any proximity-effect correction. A small deviation from the theory is thus expected. All values are comparable to those found in [4]. The large coupling coefficients dictate the wide resonance widths, as well as the stop-band width. It is apparent that losses are considerably higher on the low-frequency band for both groups of devices, as expected from the band diagrams. An inspection of Fig. 2(b) reveals that etched holes barely extend past 1μm below the quaternary layer and become conical in the bottom; some sidewall roughness is also visible. These features cause large out-of-plane radiation that is directly related to the high loss figures [7]. Reflection and group delay curves were obtained with the same parameters. In all cases, a good agreement with experimental curves is observed.

Despite the mild group delay enhancement, calculated GVD from CMT reaches $D \approx -8.5\times10^{6}$ps/km·nm on the high-frequency band-edge for the device in Fig. 4(b), almost five orders of magnitude that of dispersion-compensating fiber [2]; this corresponds to a total dispersion of -0.7ps/nm for the 80-μm waveguide. The bandwidth over which the dispersion remains within the same order of magnitude is slightly larger than 1.0nm, pointing towards possible uses of similar PC waveguides in dispersion compensation or pulse-shaping by proper tuning of the coupling coefficient and lattice constant. Considering the same parameters and zero loss, the maximum achievable excess delay and largest total dispersion are respectively 1.06ps, and -1.2ps/nm. On the other hand, it must be noted that the large dispersion figures reported here can in principle be found in any one-dimensional system with very large coupling coefficients. Photonic crystal waveguides naturally offer such characteristic, given the large index discontinuities and very narrow confinement regions.

A very detailed theoretical account on the usage of the described 1D band-edge effects for dispersion compensation, including impairment due to high-order dispersion, is given in references [19, 20].

5. Summary and conclusions

A set of InP-based test devices were fabricated to characterize deeply-etched Photonic Crystal structures. The fabrication process is a novel form of integration of deeply-etched PC with standard photonic integrated circuit structures. Etched PC holes were more than 2μm deep, with aspect ratio close to 9. The devices incorporated PC patterns and standard ridge waveguides with electrical contacts. This allowed fast and complete polarization-resolved measurement of transmission, reflection and group delay characteristics of a series of $W3^{(M)}$ PC waveguides.

Waveguide transmission and reflection measurements revealed a small stop-band for TM-polarized modes. Measured excess group delay curves displayed a maximum enhancement of approximately 0.6ps (~60% over that from a ridge waveguide of the same length) at the edge of the stop-band. Group-Velocity Dispersion of almost five orders of magnitude that of dispersion-compensating fiber was observed in the same region. Experimental curves were fitted with coupled-mode theory, yielding estimates for losses and coupling coefficient. Enhancement of group delay and GVD is clearly dependent on propagation losses. Even at zero loss, though, only a mild enhancement of group delay is found. On the other hand, dispersion is found to be extremely large over reasonably wide bandwidths, even when considerable losses are present. This suggests that, by proper tuning of coupling coefficients, very compact dispersion-compensating or pulse-shaping elements could be designed.

Acknowledgments

This work was supported by the Center for Nanosystems Innovation for Defense (CNID) award DMEA90-02-2-0215, jointly funded by DMEA and DARPA.

#7340 - $15.00 USD Received 2 May 2005; revised 10 June 2005; accepted 13 June 2005